Wenfeng Xia *Editor*

Biomedical Photoacoustics

Technology and Applications

Springer

Biomedical Photoacoustics

Wenfeng Xia
Editor

Biomedical Photoacoustics

Technology and Applications

Springer

Editor
Wenfeng Xia
School of Biomedical Engineering &
Imaging Sciences
King's College London
London, UK

ISBN 978-3-031-61410-1 ISBN 978-3-031-61411-8 (eBook)
https://doi.org/10.1007/978-3-031-61411-8

This Springer imprint is published by the registered company Springer Nature Switzerland AG
The registered company address is: Gewerbestrasse 11, 6330 Cham, Switzerland

Preface

Biomedical Photoacoustics: Technology and Applications invites you into the dynamic realm of photoacoustic imaging and sensing, an exciting field where optics, acoustics, and biomedical sciences converge. At its core, photoacoustic imaging, also known as optoacoustic imaging, harnesses the interaction between light and tissue to produce high-resolution, anatomical, molecular, and functional images with remarkable depth penetration. This hybrid modality, utilising the generation and detection of ultrasound waves induced by pulsed or modulated light, offers a powerful synthesis of optical and ultrasound techniques.

The exponential growth of photoacoustic imaging over the past two decades underscores its transformative potential in biomedical research and clinical practice. Continuous advancements in hardware, software, and contrast agents have expanded its capabilities and applications. Chapters 1, 2, and 3 delve into innovations in imaging systems, including microscopy, tomography, and endoscopy, enabling high-resolution imaging across various scales and unprecedented access to inaccessible body areas. Furthermore, Chaps. 4 and 5 review recent advancements in model-based reconstructions and deep learning algorithms, enhancing image quality and speed, and facilitating real-time and quantitative imaging in clinical settings.

The integration of novel contrast agents, discussed in Chap. 6, has enabled deep-tissue molecular imaging and targeted therapy monitoring, particularly in oncology and cardiovascular medicine. Technical validation methodologies, as outlined in Chap. 7, have ensured the reliability and reproducibility of photoacoustic imaging systems, vital for their clinical translation.

Chapters 8, 9, 10, and 11, comprising the Emerging Techniques in Photoacoustics section, illuminate novel approaches such as optical wavefront shaping and optical ultrasound sensors and devices, showcasing the innovative frontier of photoacoustic imaging. Additionally, Chaps. 12 and 13 emphasise the compatibility and complementarity of photoacoustic imaging with established clinical modalities and emerging techniques, positioning it as a promising tool for integration into routine clinical practice. Chapters 14, 15, 16, 17, 18, 19, 20, 21, and 22 encompass a wide range of preclinical and clinical applications, from cancer research and bacterial cell identification to tissue characterisation, brain imaging, and surgical guidance.

Together, these chapters underscore the versatility and promising prospects of photoacoustic imaging in biomedical research and clinical practice.

Born out of a collective aspiration to bridge the gap between theory and practice, this book aims to meet the growing demand for a comprehensive resource encapsulating the latest technologies, methodologies, and applications in photoacoustic imaging. As the editor, I am inspired by the rapid pace of innovation and the expanding horizons in this field, recognising the necessity of consolidating this wealth of knowledge into a single volume that can serve as a guiding beacon for researchers, practitioners, and students alike.

Tailored for a diverse audience encompassing postgraduate students and researchers across physics, engineering, biomedical sciences, and clinical disciplines, this book serves as a vital link between theoretical understanding and practical application in photoacoustic imaging. Whether you are embarking on your journey into this dynamic field or seeking to deepen your existing knowledge and expertise, this volume stands as a reservoir of information and inspiration, poised to propel you forward in your pursuits.

I extend my heartfelt gratitude to the contributors for their generous sharing of expertise and perspectives. I also express my appreciation to the team at Springer Nature, especially senior editor Merry Stuber and production editor Vinodhini Srinivasan, for their dedication and support in bringing this project to fruition.

It is my sincere hope that *Biomedical Photoacoustics: Technology and Applications* will serve as a catalyst for further exploration, collaboration, and innovation in photoacoustic imaging, ultimately leading to advancements that enhance healthcare outcomes and improve the quality of life for patients worldwide.

London, UK Wenfeng Xia

Contents

Contributors

Sean Aleman Department of Medical Engineering, University of South Florida, Tampa, FL, USA

Navchetan Awasthi Department of Biomedical Engineering, Eindhoven University of Technology, Eindhoven, The Netherlands
Informatics Institute, University of Amsterdam, Amsterdam, The Netherlands
Department of Biomedical Engineering and Physics, Amsterdam UMC, Amsterdam, The Netherlands

Semyon Bodian Department of Chemistry, University College London, London, UK
Department of Medical Physics and Biomedical Engineering, University College London, London, UK

Yingna Chen Institute of Acoustics, School of Physics Science and Engineering, Tongji University, Shanghai, China
College of Science and Technology, Ningbo University, Zhejiang, China

Zhenyue Chen Institute for Biomedical Engineering and Institute of Pharmacology and Toxicology, Faculty of Medicine, University of Zurich, Zurich, Switzerland
Institute for Biomedical Engineering, Department of Information Technology and Electrical Engineering, ETH Zurich, Zurich, Switzerland

Qian Cheng Institute of Acoustics, School of Physics Science and Engineering, Tongji University, Shanghai, China

Adrien E. Desjardins Department of Medical Physics and Biomedical Engineering, University College London, London, UK
Wellcome/EPSRC Centre for Interventional and Surgical Sciences, University College London, London, UK

Robert H. Edgar Department of Bioengineering, University of Pittsburgh, Pittsburgh, PA, USA

Bangxu Fan College of Future Technology, Peking University, Beijing, China

Ting Feng Institute of Acoustics, School of Physics Science and Engineering, Tongji University, Shanghai, China
Academy for Engineering and Technology, Fudan University, Shanghai, China

Kalloor Joseph Francis Faculty of Science and Technology, University of Twente, Enschede, The Netherlands

Ya Gao Institute of Acoustics, School of Physics Science and Engineering, Tongji University, Shanghai, China

Damien Gasteau Multi-Modality Medical Imaging group (M3I), Technical Medical Centre, University of Twente, Enschede, The Netherlands

Irmak Gezginer Institute for Biomedical Engineering and Institute of Pharmacology and Toxicology, Faculty of Medicine, University of Zurich, Zurich, Switzerland
Institute for Biomedical Engineering, Department of Information Technology and Electrical Engineering, ETH Zurich, Zurich, Switzerland

Amir Gholampour Department of Biomedical Engineering, Eindhoven University of Technology, Eindhoven, The Netherlands

Katherine Gisi Department of Electrical and Computer Engineering, Iowa State University, Ames, IA, USA

Lina Hacker Department of Oncology, University of Oxford, Oxford, UK

Andreas Hauptmann Research Unit of Mathematical Sciences, University of Oulu, Oulu, Finland
Department of Computer Science, University College London, London, UK

Bingxin Huang Translational and Advanced Bioimaging Laboratory, Department of Chemical and Biological Engineering, Hong Kong University of Science and Technology, Clear Water Bay, Hong Kong, China

Lucas Humayun Department of Biomedical Engineering, Duke University, Durham, NC, USA

Fumiyuki Ichihashi Research and Development Division, CYBERDYNE INC, Tsukuba, Japan

Michael Jaeger Optoacoustic Imaging Group, University of Bern, Bern, Switzerland

Huabei Jiang Department of Medical Engineering, University of South Florida, Tampa, FL, USA

James Joseph School of Science and Engineering, University of Dundee, Dundee, UK

Chulhong Kim Pohang University of Science and Technology, Department of Electrical Engineering, Convergence IT Engineering, Medical Science and Engineering, Mechanical Engineering, School of Interdisciplinary Bioscience and

Bioengineering, Graduate School of Artificial Intelligence, Medical Device Innovation Center, Pohang, Republic of Korea

Kaitlyn Kim Department of Biomedical Engineering, University of California, Irvine, CA, USA

Jiayan Li Institute of Acoustics, School of Physics Science and Engineering, Tongji University, Shanghai, China

Teng Liu School of Electronic and Optical Engineering, Nanjing University of Science and Technology, Nanjing, China

Richard G. P. Lopata Department of Biomedical Engineering, Eindhoven University of Technology, Eindhoven, The Netherlands

Jun Ma Guangdong Provincial Key Laboratory of Optical Fiber Sensing and Communications, Institute of Photonics Technology, Jinan University, Guangzhou, China

Srivalleesha Mallidi Department of Biomedical Engineering, Tufts University, Medford, MA, USA
Wellman Center for Photomedicine, Massachusetts General Hospital, Harvard Medical School, Boston, MA, USA

Srirang Manohar Multi-Modality Medical Imaging group (M3I), Technical Medical Centre, University of Twente, Enschede, The Netherlands

Shuai Na College of Future Technology, Peking University, Beijing, China

Sacha Noimark Department of Chemistry, University College London, London, UK
Department of Medical Physics and Biomedical Engineering, University College London, London, UK
Wellcome EPSRC Institute of Surgical Science, University College London, London, UK

Donghyeon Oh Pohang University of Science and Technology, Department of Electrical Engineering, Convergence IT Engineering, Medical Device Innovation Center, Pohang, Republic of Korea

Byullee Park Sungkyunkwan University, Department of Biophysics, Institute of Quantum Biophysics, Suwon, Republic of Korea

Ivan P. Parkin Department of Chemistry, University College London, London, UK

Vijitha Periyasamy Department of Electrical and Computer Engineering, Iowa State University, Ames, IA, USA

Manojit Pramanik Department of Electrical and Computer Engineering, Iowa State University, Ames, IA, USA

Menglu Qian Institute of Acoustics, School of Physics Science and Engineering, Tongji University, Shanghai, China

Nastaran Mohammadian Rad Department of Biomedical Engineering, Eindhoven University of Technology, Eindhoven, The Netherlands
Department of Precision Medicine, Maastricht University, Maastricht, The Netherlands

Daniel Razansky Institute for Biomedical Engineering and Institute of Pharmacology and Toxicology, Faculty of Medicine, University of Zurich, Zurich, Switzerland
Institute for Biomedical Engineering, Department of Information Technology and Electrical Engineering, ETH Zurich, Zurich, Switzerland
Zurich Neuroscience Center (ZNZ), Zurich, Switzerland

Qiangzhou Rong Department of Biomedical Engineering, Duke University, Durham, NC, USA

Yoshiyuki Sankai Research and Development Division, CYBERDYNE INC, Tsukuba, Japan

Deeksha Sankepalle Department of Biomedical Engineering, Tufts University, Medford, MA, USA

Naoto Sato Research and Development Division, CYBERDYNE INC, Tsukuba, Japan

Yuecheng Shen School of Electronics and Information Technology, Sun Yat-sen University, Guangzhou, China

Mengjie Shi School of Biomedical Engineering & Imaging Sciences, King's College London, London, UK

Mithun Kuniyil Ajith Singh Research and Business Development Division, CYBERDYNE INC, Rotterdam, the Netherlands

Allison Sweeney Department of Biomedical Engineering, Tufts University, Medford, MA, USA

Dean Ta Department of Electronic Engineering, Fudan University, Shanghai, China

Tanja Tarvainen Department of Technical Physics, University of Eastern Finland, Kuopio, Finland
Department of Computer Science, University College London, London, UK

David Thompson Multi-Modality Medical Imaging group (M3I), Technical Medical Centre, University of Twente, Enschede, The Netherlands

Tom Vercauteren School of Biomedical Engineering & Imaging Sciences, King's College London, London, UK

John A. Viator Department of Bioengineering, University of Pittsburgh, Pittsburgh, PA, USA
Department of Engineering, Duquesne University, Pittsburgh, PA, USA

Simeon J. West Department of Anaesthesia, University College Hospital, London, UK

Ivy H. M. Wong Translational and Advanced Bioimaging Laboratory, Department of Chemical and Biological Engineering, Hong Kong University of Science and Technology, Clear Water Bay, Hong Kong, China

Terence T. W. Wong Translational and Advanced Bioimaging Laboratory, Department of Chemical and Biological Engineering, Hong Kong University of Science and Technology, Clear Water Bay, Hong Kong, China

Min Wu Department of Biomedical Engineering, Eindhoven University of Technology, Eindhoven, The Netherlands

Shiying Wu Institute of Acoustics, School of Physics Science and Engineering, Tongji University, Shanghai, China

Jun Xia Department of Biomedical Engineering, University at Buffalo, The State University of New York, Buffalo, NY, USA

Wenfeng Xia School of Biomedical Engineering & Imaging Sciences, King's College London, London, UK

Shawn (Liangzhong) Xiang Department of Biomedical Engineering, University of California, Irvine, CA, USA
Beckman Laser Institute & Medical Clinic, University of California, Irvine, CA, USA
Department of Radiological Sciences, University of California, Irvine, CA, USA

Weiya Xie Institute of Acoustics, School of Physics Science and Engineering, Tongji University, Shanghai, China

Wenyi Xu Institute of Acoustics, School of Physics Science and Engineering, Tongji University, Shanghai, China

Hao Yang Department of Medical Engineering, University of South Florida, Tampa, FL, USA

Junjie Yao Department of Biomedical Engineering, Duke University, Durham, NC, USA

Huijuan Zhang Department of Biomedical Engineering, University at Buffalo, The State University of New York, Buffalo, NY, USA

Jinyan Zhang College of Future Technology, Peking University, Beijing, China

Mengjiao Zhang Institute of Acoustics, School of Physics Science and Engineering, Tongji University, Shanghai, China

Yan Zhang Translational and Advanced Bioimaging Laboratory, Department of Chemical and Biological Engineering, Hong Kong University of Science and Technology, Clear Water Bay, Hong Kong, China
School of Applied and Engineering Physics, Cornell University, Ithaca, NY, USA

Tianrui Zhao School of Biomedical Engineering & Imaging Sciences, King's College London, London, UK

Emily Zheng Department of Biomedical Engineering, University at Buffalo, The State University of New York, Buffalo, NY, USA

Quanyu Zhou Institute for Biomedical Engineering and Institute of Pharmacology and Toxicology, Faculty of Medicine, University of Zurich, Zurich, Switzerland
Institute for Biomedical Engineering, Department of Information Technology and Electrical Engineering, ETH Zurich, Zurich, Switzerland

Part I
Principles and Imaging Systems

Chapter 1
Photoacoustic Microscopy

Qiangzhou Rong, Lucas Humayun, and Junjie Yao

Abstract Biomedical imaging allows us to explore the complex biology of living organisms and better understand the clinical progression of diseases through the visualization of dynamic, functional, and molecular events. Among the modern biomedical imaging technologies, photoacoustic microscopy (PAM) provides unique optical absorption contrast and high-spatial resolution at depths beyond the penetration limit of traditional optical microscopy. Over the last decades, PAM has become an increasingly popular anatomical, functional, and molecular information. In this book, we introduce the basic principles and typical system designs of PAM, including optical-resolution PAM and acoustic-resolution PAM. We also discuss the common characteristics of PAM, including spatial resolutions, penetration depth, PA signal detectors, and the scanning approach. Finally, we present the major biomedical applications of PAM, including functional measurement, anatomical imaging from cellular to organismal level, label-free functional imaging using endogenous biomolecules, molecular imaging using exogenous contrast agents, and preclinical and clinical applications.

Keywords Photoacoustic imaging · Molecular imaging · Targeted contrast agent · Preclinical and clinical applications

1.1 Introduction

Biomedical imaging first rose to popularity when medical professionals began using X-ray to diagnose and detect fractures in foreign bodies [1–7]. Thanks to its unique ability to visualize biological structures and function in vivo, biomedical imaging has become a staple in patient care [8–11]. Today, some of the most common biomedical imaging modalities include digital X-ray radiography [12],

Q. Rong · L. Humayun · J. Yao (✉)
Department of Biomedical Engineering, Duke University, Durham, NC, USA
e-mail: junjie.yao@duke.edu

W. Xia (ed.), *Biomedical Photoacoustics*,
https://doi.org/10.1007/978-3-031-61411-8_1

X-ray computed tomography (CT) [13], nuclear imaging (e.g., positron emission tomography (PET) and single photon emission computed tomography (SPECT)) [14], ultrasound imaging [15], optical imaging [16] and magnetic resonance imaging (MRI) [17]. Optimization of these modalities as well as the development of new imaging technologies have even shown potential to capture visual data of microscopic objects while maintaining high resolution [18–21]. As biomedical imaging continues to expand our understanding of tissue composition, morphology, function, and dynamic biological processes, it has become a necessity for pushing the boundaries of scientific inquiry.

Optical imaging is a unique branch of the biomedical imaging family and has taken great strides over the past two decades [22–24]. Thanks to their characteristic high resolution, high sensitivity, specificity, and practicality, optical imaging techniques are currently able to offer information ranging from a large 3D bulk to finite molecular-grade information (e.g., cancer biomarkers, cell metabolic state, and atherosclerotic lesions). These features align well with the increased demand for personalized health care envisaged for diagnosing patient subpopulations with increased precision [25]. Indeed, optical diagnostic imaging is already proving to revolutionize clinical care [26].

One of the main challenges facing optical imaging is strong light scattering in biological tissue as this decreases spatial resolution and restricts imaging depth [27–31]. Fortunately, several developing optical imaging modalities, including, confocal microscopy [32], two-photon microscopy [33, 34], and optical coherence tomography (OCT) [35–37] offer higher-resolution images. Through the detection of singly backscattered photons for OCT processing and ballistic photons these technologies appear to alleviate the challenge of maintaining high image quality. Unfortunately, by increasing resolution, these optical imaging techniques sacrifice depth, evidenced by their typical limitation to less than 1 mm of penetration. Beyond this limit, existing modalities are unable to produce meaningful visualizations. While researchers have made a tremendous effort to overcome the hurdle of imaging depth [38, 39] through the development of technologies such as diffuse optical tomography (DOT), optical imaging alone is largely unable to achieve depth-dependent spatial resolution.

Photoacoustic imaging (PAI), or optoacoustic imaging (OAI), is a hybrid imaging modality that merges optical illumination and ultrasound detection [40–42]. In the last two decades, PAI has attracted attention for its biomedical pre-clinical and clinical applications. PAI first relies on a pulsed laser with pico-second or nano-second cycles to illuminate the biological sample. The sample then absorbs the laser-derived optical energy and converts it into heat, making local temperature rise. The subsequent thermoelastic expansion results in the release of US waves. US signals can be collected by a range of sensors including piezoelectric transducers and optical interferometers [43, 44].

In contrast to other optical imaging techniques, PAI relies on the detection of US waves, which undergoes less scattering and attenuation in tissue. PAI can therefore image deeper targets with better resolution than comparable optical imaging modalities [45, 46]. In order to deliver clinically relevant information,

PAI apparatuses are often designed to target biomaterial with the intrinsic optical absorption of chromophores, such as hemoglobin, melanin, lipids, and water [47, 48]. Thanks to the adaptability of the pulsed laser component of PAI, each of these targets can be utilized to capture physiological data simply by adjusting the laser's emitted range of wavelengths [49, 50]. In addition, the label-free nature of endogenous contrast PAI makes it appropriate for patients' compliance in long-term longitudinal monitoring.

The PA effect was initially discovered by Alexander Bell in 1880 [51], who observed a correlation between acoustic energy emission frequency and light modulation frequency when light energy was rapidly interrupted while illuminating different solid substances. This discovery electrified the field of light-induced sonorous effects, attracting many notable scientists to develop theories and conduct further experimental studies [52–54]. This early research was instrumental in constructing the foundations of modern PAI. The subsequent development of related optical and acoustic technologies, such as effective and affordable laser sources [55, 56], miniaturized US detection devices [57, 58], novel computational platforms and advanced inversion models [59–61], and refined PAI, making it a valuable tool for modern biological research of clinical diagnostic techniques.

Today, the field of PAI can be well divided into two categories: photoacoustic computed tomography (PACT) [62] and photoacoustic microscopy (PAM) [63]. PACT can provide deep penetration up to several centimeters with high spatial resolution (hundreds of micrometers) by using wide-field optical illumination and parallel acoustic detection [64, 65]. In contrast, PAM can provide high spatial resolution (several micrometers), but it sacrifices penetration depth (one to several millimeters) by using a co-focused optical illumination and acoustic detection method [66]. When used together, PACT and PAM systems offer extremely valuable visualization data with many biomedical applications [66, 67]. While PACT is an equally exciting and valuable field of PAI, we will primarily discuss the PAM system in this chapter.

PAM is implemented by a confocal microscopy method of optical excitation and acoustic detection. The confocal configuration can offer large detection sensitivity and high SNR. According to the size of the focused laser spot on the target, the PAM system can be divided into two groups: optical-resolution PAM (OR-PAM) [68] and acoustic-resolution PAM (AR-PAM) [69]. In OR-PAM, the illuminating light is tightly focused as a source so that the spot size of focused light significantly determines the system's lateral resolution by $0.51 \times \lambda_0 = \mathrm{NA}_0$ [70, 71], where λ_0 is the wavelength of light and NA_0 is the numerical aperture (NA) of the optical objective. For example, when using an objective with NA of 0.1 and light wavelength of 532 nm, the OR-PAM can offer a resolution of 3 μm. However, due to the limited light penetration, the imaging depth of OR-PAM is approximately 1 mm. In AR-PAM, the illuminated light is weakly focused or collimated; thus, the optical beam spot is larger than the focal spot of acoustic detection. In contrast to OR-PAM, the lateral resolution of AR-PAM relies heavily on the spot size of acoustic detection [72], which can be calculated by the equation of $0.71 \times \lambda_a = \mathrm{NA}_a$ where λ_a is the wavelength of the acoustic wave and NA_a is the NA of the focused

ultrasonic transducer. In comparison to OR-PAM, AR-PAM lateral resolution is more than ten times worse. In addition, the bandwidth of the ultrasonic detector determines the axial resolutions of OR- and AR-PAM that can be calculated by the equation of $0.88 \times c/(\Delta f)$, where c is the US speed, and Δf is the response frequency bandwidth of the transducer. For in vivo studies, it is necessary that the optical fluence determined by the optical spot size is lower than the maximum permissible exposure (MPE) regulated by American National Standard for Safe Use of Lasers [73]. This limitation allows much larger pulse energy in AR-PAM and therefore achieves larger penetration depth. It is because PA signals suffer from tissue attenuation that the acoustic penetration depth of AR-PAM system is inversely proportional to the central frequency of the transducer [74]. The large field of view (FOV) of PAM system is usually realized by scanning methods, including moving the sample or the light/sound [75, 76]. The conventional scanning method requires advancing through stepper motor stages with considerable speed. In order for high-quality imaging, the step size of the motor should be at most half of the lateral resolution. However, imaging a large FOV takes time. There have been other developed methods to improve the imaging speed, including the use of commercial Galvanometer mirrors [77], micro-electromechanical system (MEMS) scanning mirrors [76], and multiple-surface polygon mirrors [78].

Despite some of the challenges it currently faces, PAM presents itself as a versatile tool that can accurately detect endogenous and exogenous [48, 79] targets at their absorbing wavelengths better than fluorescence-based methods [80, 81], such as wide-field, confocal, and multi-photon microscopy. Its additional utility in capturing anatomical, functional, molecular, flow dynamic, and metabolic contrasts in vivo makes it an important tool for future scientific study and clinical diagnoses.

1.2 Basics of PAI

1.2.1 General Behavior of Light in Biological Tissue

Most biological tissues exhibit strong optical scattering. Thus, tissue samples used in optical imaging are commonly referred to as scattering or turbid media [82, 83]. While optical scattering is generally quite extensive in biological tissue, optical absorption is relatively weak with absorption in the range of 400–1350 nm. The mean free path between photon scattering is on the order of 0.1 nm, and the mean absorption length is from 10 nm to 100 nm. Figure 1.1 in Ref. [40, 82] displays the schematic of photon propagation in biological tissue. Here the light source employs a temporally Dirac delta pulse with a shape of a pencil beam or an infinitely narrow collimated beam. The optical properties of tissue significantly determine the light propagation in tissue as described above. For example, when using the parameters of absorption coefficient $\mu_a = 1.4\,\mathrm{cm}^{-1}$, scattering coefficient $\mu_a = 350\,\mathrm{cm}^{-1}$, scattering anisotropy $g = 0.8$, and refractive index $n = 1.37$, the mean free path

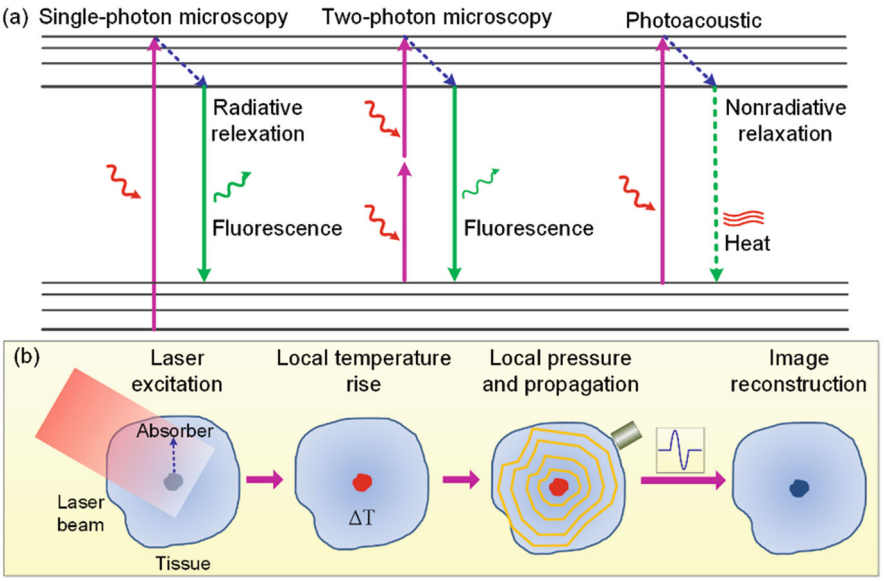

Fig. 1.1 Photon imaging principle. (**a**) Jablonski diagram, photon energy transfer in one-photon fluorescence microscopy, two-photon fluorescence microscopy, and photoacoustic generation. (**b**) basic principle of PAI [40]

is equal to 28 μm with respect to 0.6 ps propagation time. For most optical imaging, the diffusion-like behavior of light is always a key challenge. There have been various methods using various system configurations to contend with the diffusion influence.

1.2.2 Photons Absorption in Tissue

A given photon's absorption is normally characterized by the absorption coefficient μ_a or the probability of photon being absorbed in a medium per unit path length (e.g., 0.1 cm to 1 cm in biological tissue) [84–87]. The mean absorption length can be calculated by taking the reciprocal of μ_a. The absorption cross-sectional area (σ_a) can characterize the absorbing capability of a single absorber. σ_a is related to its geometric cross-sectional area σ_g by the absorption efficiency expression $Q_a : \sigma_a = Q_a \sigma_g$. The density of absorbers within a given volume is represented by N_a; therefore, the absorption coefficient can be calculated by summing the total cross-sectional area. Assuming the absorbers are independent of one another, the μ_a per unit volume can be given by:

$$\mu_a = N_a \sigma_a \tag{1.1}$$

As light propagates in an absorbing-only tissue, its attenuation can be calculated by

$$\frac{dI}{I} = -\mu_a dx \tag{1.2}$$

where I is the light intensity, and x is the distance the light travels. Equation (1.2) displays the percentages of absorbed light in interval $(x,\ x + dx)$. When integrated, invoking Beer's Law yields the following expression

$$I(x) = I_0 \exp(-\mu_a x) \tag{1.3}$$

where I_0 is the light intensity at $x = 0$. This equation is effective even for a tortuous path. Transmittance is defined by

$$T(x) = \frac{I(x)}{I_0} \tag{1.4}$$

Equation (1.4) can be used for the probability of survival after propagation over x.

Within the context of biological tissue, optical absorption is primarily caused by hemoglobin, melanin, and water. Figure 1.2a displays the absorption spectrum of some primary absorbing biological tissue components. In the figure, the absorption coefficients are plotted as a function of wavelengths. This provides an important reference for the laser source option to improve the PA signal. Because of their dramatically different optical absorbing properties, the reported detection sensitivity (NEC) for exogenous contrast agents varies from millimolar to picomolar. Roughly, the reported NEC is on the level of millimolar for microbubbles, micromolar for organic dyes, picomolar for nanoparticles, and nanomolar for fluorescent proteins [85]. Figure 1.2b summarizes the reported PAM detection sensitivity (NEC) of representative endogenous and exogenous contrast agents.

As mentioned above, the oxy- and deoxyhemoglobin present different absorption wavelengths (e.g., 532 nm and 558 nm) but have a few intersections, termed isosbestic points. At these points, the two types of hemoglobin's absorption coefficients are therefore only relative to the total concentration. The concentrations of two kinds of hemoglobin can be obtained as follows:

$$\mu_a(\lambda_1) = \ln(10)\varepsilon_{\text{ox}}(\lambda_1) C_{\text{ox}} + \ln(10)\varepsilon_{\text{de}}(\lambda_1) C_{\text{de}} \tag{1.5}$$

$$\mu_a(\lambda_2) = \ln(10)\varepsilon_{\text{ox}}(\lambda_2) C_{\text{ox}} + \ln(10)\varepsilon_{\text{de}}(\lambda_2) C_{\text{de}} \tag{1.6}$$

where λ_1 and λ_2 are the two corresponding wavelengths, ε_{ox} and ε_{de} are the known molar extinction coefficient of oxy- and deoxyhemoglobin, C_{ox} and C_{de} are the molar concentrations of oxy- and deoxyhemoglobin, respectively, in the tissue. According to the Eqs. (1.4) and (1.6), the oxygen saturation (sO_2) and the total

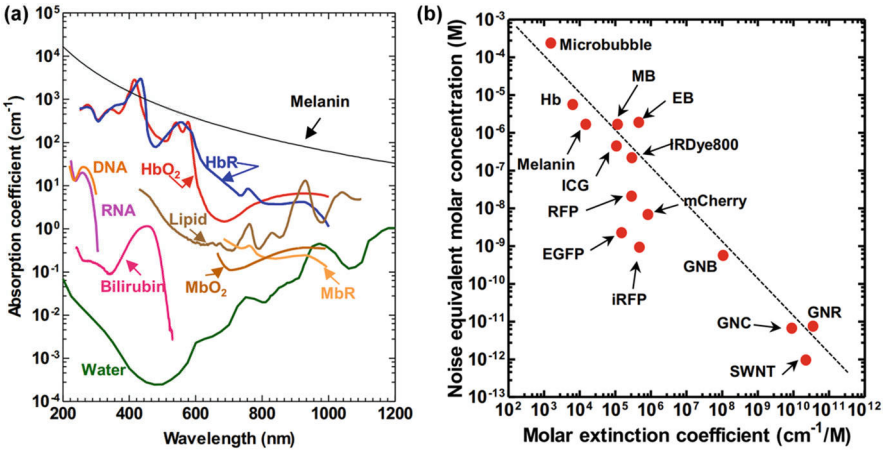

Fig. 1.2 (**a**) Absorption spectra of major endogenous contrast agents in biological tissue at normal concentrations. (**b**) reported noise equivalent molar concentrations (NEC) of major endogenous and exogenous contrast agents, versus their molar extinction coefficients. Due to the lack of complete information, the incident fluence is not corrected here. HbO_2 oxy-hemoglobin, HbR deoxy-hemoglobin, MbO_2 oxymyoglobin, MbR reduced myoglobin, EB evens blue, EGFP enhanced green fluorescent protein, GNB gold nanobeacon, GNC gold nanocage, GNR gold nanorod, Hb hemoglobin, ICG indocyanine green, IRDye800 near-infrared Dye800, iRFP near-infrared red fluorescent protein, MB methylene blue, mCherry monomeric cherry protein; Melanin; RFP red fluorescent protein, SWNT single walled nanotube. (Reprinted with permission from [85] for (a) and (b))

concentration (C_{Hb}) of hemoglobin can be calculated by the C_{ox} and C_{de}, which can be expressed as [88–90].

$$\mathrm{SO}_2 = \frac{C_{\mathrm{ox}}}{C_{\mathrm{ox}} + C_{\mathrm{de}}} \tag{1.7}$$

$$C_{\mathrm{Hb}} = C_{\mathrm{ox}} + C_{\mathrm{de}} \tag{1.8}$$

This theoretical analysis can be used for understanding the pulse oximetry and functional imaging. For example, C_{Hb} rising can analyze angiogenesis, whereas sO_2 decreasing can predict tumor hypermetabolism.

1.2.3 Photon Scattering in Tissue

Light scattering effect can be modeled by the Mie theory and the Rayleigh theory if the light wavelength is much larger than the scattering spherical particle [82, 91–95]. As thousands of obstacles are randomly assorted throughout a medium, the

scattering of photons should also be expected to occur randomly. If we assume that obstacles are sparsely distributed throughout a tissue medium, scattering events can also be assumed to be independent, thus the single-scattering theory can be invoked to characterize photon scattering. The following discussion details a mathematical implementation of a sparse model, permitting the use of single-scattering theory. The scattering coefficient μ_s is defined as the probability of photon scattering in a medium per unit path length. In biological tissue, μ_s has a representative value of 100 cm^{-1}, and μ_s's reciprocal is referred to as the scattering mean free path. For a single scatter, the scattering cross-section σ_s, which indicates the area across which scattering can occur, is related to its geometric cross-sectional area σ_g by the scattering efficiency $Q_s : \sigma_s = Q_s \sigma_g$. The scattering coefficient of a given medium is related to σ_s by the number of obstacles per unit volume (N_s), which can be expressed as

$$\mu_s = N_s \sigma_s \tag{1.9}$$

After a photon propagates over path length x, the probability of no scattering (or ballistic transmittance T) can be expressed by Beer's law as

$$T(x) = \exp(-\mu_s x) \tag{1.10}$$

There are two factors that strongly influence photon scattering: biological structure size concordance with the optical wavelength and refractive index discordance with the surrounding medium [96–99]. Interestingly, each component of biological tissue presents a different refractive index: 1.35–1.36 for extracellular fluid, 1.36–1.375 for cytoplasm, and 1.38–1.41 for nuclei and mitochondria. The difference in refractive indices ultimately contributes to the highest degree of scattering.

The total interaction-induced extinction coefficient μ_t is the sum of the absorption coefficient and scattering coefficient, which can be expressed as

$$\mu_t = \mu_a + \mu_s \tag{1.11}$$

Finally, the mean free path between interaction events can be computed by taking the reciprocal of μ_t (Fig. 1.3).

1.2.4 Light Transport Through Tissue

Light transport in tissue can be characterized by two kinds of models: an essentially discrete model of individual photon interactions that can be analyzed by a Monte Carlo method and a continuous model based on a differential equation approximation that can be analyzed by the diffusion equation [100–102]. These two methods can be derived by an integro-differential equation expressed as

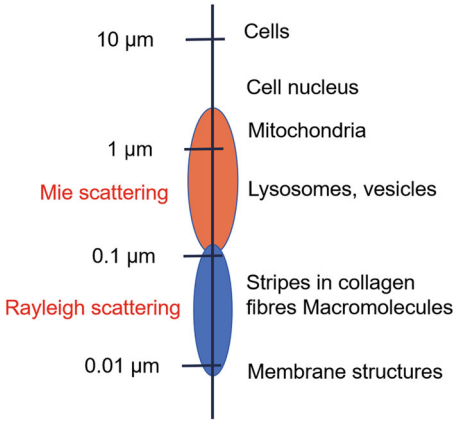

Fig. 1.3 Biological structures of various sizes for photon scattering [99]

$$\left\{\hat{\mathrm{s}}\cdot\nabla+\mu_{\mathrm{a}}+\mu_s+\frac{1}{\nu}\frac{\partial}{\partial t}\right\}\phi\left(r,\hat{\mathrm{s}}',t\right)=\frac{1}{\nu}q\left(\hat{\mathrm{s}},\hat{r},t\right)+\mu_s\int f\left(\hat{\mathrm{s}}',\hat{\mathrm{s}}\right)\phi\left(r,\hat{\mathrm{s}}',t\right)d^2\hat{\mathrm{s}} \tag{1.12}$$

where μ_a, μ_s are absorption and scattering coefficients, respectively, $\hat{r}$,$\hat{s}$,$\hat{s}'$ are direction vectors, ν is the speed of light in the medium, $\phi\left(r,\hat{s}',t\right)$ is the photon density in direction $\hat{s}'$,q is the source term, and $f\left(\hat{s}',\hat{s}\right)$ is the probability of scattering from direction $\hat{s}'$, into direction $\hat{s}$.

Photon diffusion approximation in a second-order partial differential equation can characterize the time behavior of photon fluence rate distribution in a medium with low absorption but high scattering [103, 104]. Compared with diffusion equation in physics, the photon diffusion equation has an absorption term, which can be expressed as

$$\left\{\nabla\cdot\kappa\nabla-\mu_{\mathrm{a}}c-\frac{\partial}{\partial t}\right\}\Phi\left(r,t\right)=-q_0\left(r,t\right) \tag{1.13}$$

where Φ is the photon fluence rate, q_0 is the source term, and $\kappa(r)$ is the diffusion coefficient. The mathematical form of $\kappa(r)$ can be written as

$$\kappa=\frac{\nu}{3\left(\mu_a+(1-g)\,\mu_s\right)} \tag{1.14}$$

where g is the average cosine of the scattering angle distribution and $(1-g)\mu_s$ can also be represented by the reduced scattering coefficient μ_{s}'.

The photon fluence rate can be calculated by

$$\Phi\left(r,t\right)=\int\phi\left(r,\hat{s}',t\right)d^2\hat{s} \tag{1.15}$$

The Eq. (1.13) has been identified by the theory and experiment demonstrations in the case of the near-infrared (NIR) transillumination of tissue with the representative ranges $0.01 < \mu_a < 0.1\,mm^{-1}$ and $1.0 < \mu_s' < 10.0\ mm^{-1}$. It should be noted, however, in instances where the scattering effect does not dominate the light transillumination, this diffusion approximation may not be exact.

1.2.5 Acoustic Wave Modelling

In this section, we discuss an acoustic model of a fluidic region. The acoustic wave is generated when the pulse laser illuminates the sample and cause thermal expansion. The generation mechanism is based on thermoelastic effect, and the effects of viscosity and thermal conductivity could be ignored [105–107]. The acoustic pressure equation can be expressed as

$$\left\{\nabla^2 - \frac{1}{c^2}\frac{\partial}{\partial t^2}\right\} p = -\frac{\beta}{C_p}\frac{\partial H}{\partial t} \tag{1.16}$$

where c is the sound speed, β is the volume thermal expansivity, C_p is the constant pressure specific heat capacity, p is the acoustic pressure and H is the heat energy per unit volume and per unit time deposited in the fluid. p and H normally rely on the position $r = (x, y, z)$ and time t.

1.2.6 PA Effect on Tissue

In accordance with the photoacoustic mechanism mentioned above, the photoacoustic signal in biomedical tissue is highly dependent on the absorption of the pulsed laser. When absorbed light energy is transferred to thermal energy local temperature is raised, causing tissue expansion followed by sharp contraction. This process produces acoustic pressure. Thus, the generation of photoacoustic signals can be characterized by a thermodynamic energy relation and state equation [82, 107], which can be written as

$$\rho C_p \frac{\partial \tau}{\partial t} = H \tag{1.17}$$

$$p = \frac{1}{\kappa_T}\left(\frac{\delta}{\rho} + \beta\tau\right) \tag{1.18}$$

where κ_T is the isothermal compressibility, ρ is density, and τ is change in temperature. Because the illuminated light pulse is extremely short (ns) in tissue, the pressure rise associated with local temperature increase can be assumed to

occur instantaneously without expansion (i.e., adiabatic heating). This instantaneous heating brought about by pulsed laser illumination can be modeled as [105],

$$H(r,t) = H(r)\delta_D(t) \tag{1.19}$$

where $H(r)$ is the function that could describe the heat distribution per unit volume fluid (also called the absorbed energy map) and $\delta_D(t)$ is the Dirac delta. In this case, the optical energy will be absorbed before the fluid density has time to change [105]. For pressure generation to be regarded as instantaneous, the duration t_p of the pulsed laser should satisfy the condition below [106].

$$t_p \ll \frac{1}{\mu_a c} \tag{1.20}$$

Optical energy is therefore absorbed before fluid density changes. Considering the optical absorption coefficient of the medium, the spatial part of the heating function can be expressed as

$$H(r) = \mu_a(r)\Phi(r,\mu_a) \tag{1.21}$$

By the analysis above, the acoustic pressure after initial pressure distribution $p_0(r)$ is therefore proportional to the absorbed energy map.

$$p_0(r) = \left(\frac{\beta c^2}{c_p}\right) H(r) = \Gamma\mu_a(r)\Phi(r,\mu_a) \tag{1.22}$$

where Γ is the Gruneisen coefficient, a dimensionless constant that represents the efficiency of the conversion of heat to pressure.

According to Eq. (1.22), the initial pressure can be recast as an initial value problem, then propagate away as acoustic waves. Consequently, the photoacoustic wave can be performed by the equation below [107].

$$\left\{\nabla^2 - \frac{1}{c^2}\frac{\partial}{\partial t^2}\right\} p = 0,\ p|_{t=0} = p_0(r),\ \left.\frac{\partial p}{\partial t}\right|_{t=0} = 0 \tag{1.23}$$

As the linear acoustic wave propagation is modeled in the soft biological tissue, the propagation medium can be assumed to be isotropic. Therefore, the net flow does not generate and shear waves can be neglected. Three first-order equations, shown below, can be used to bridge acoustic pressure p, acoustic particle velocity u, and acoustic density δ, which correspond to the momentum conservation, mass conservation, and equation of state.

$$\frac{\partial u}{\partial t} = -\frac{1}{\rho}\nabla p,\quad \frac{\partial \delta}{\partial t} = -\rho\nabla\cdot u,\quad p = c^2\delta \tag{1.24}$$

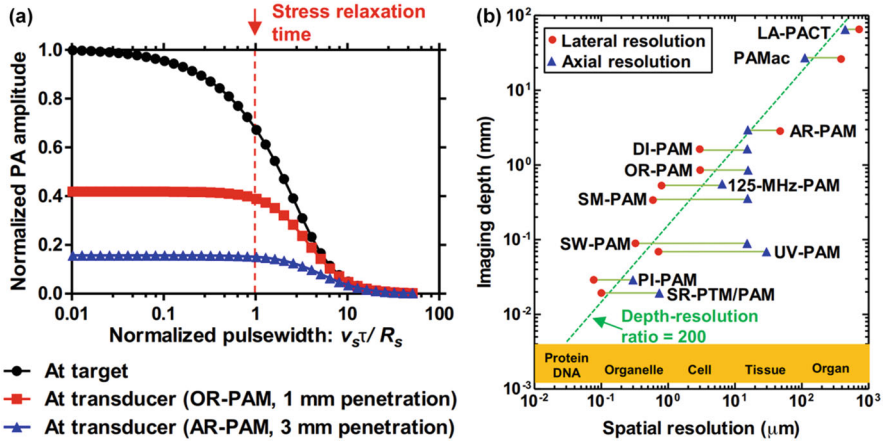

Fig. 1.4 (**a**) Simulated maximum PA pressure amplitude at the target and at the ultrasonic transducer surface as a function of the excitation pulse width in OR-PAM and AR-PAM. The excitation pulse width is normalized by the stress relaxation time, while the pulse energy is a constant. The PA amplitude of all curves is normalized by the maximum PA amplitude at the target (black curve). R_s is the axial resolution. The target is 6 mm from the transducer. In OR-PAM, the target is 1 mm under the tissue surface, while in AR-PAM the target is 3 mm under the tissue surface. Imaging depth versus spatial resolution in multi-scale photoacoustic imaging. The red circles denote lateral resolution, and the blue squares denote axial resolution. (**b**) imaging depth versus spatial resolution in multi-scale PACT. The red circles denote lateral resolution, and the blue squares denote axial resolution. DI-PAM double-illumination PAM, LA-PACT linear-array PA computed tomography, 125-MHz-PAM PAM with a 125 MHz ultrasonic transducer, PAMac deep PA macroscopy, PI-PAM photo-imprint PAM, SR-PTM/PAM super-resolution photothermal, SM-PAM submicron PAM, SW-PAM subwavelength PAM, UV-PAM ultraviolet PAM. (Reprinted with permission from [85])

This equation implies that the sound speed and ambient density rely on the position, and the pressure is related to two parameters: time and position.

The excitation pulse width is important in optimizing PA signal generation. In PAM, the stress confinement on the axial direction requires a pulse width to be less than the acoustic transit time across the resolution voxel (typically on the scale of nanoseconds). The excitation pulse width can affect the axial and lateral resolutions of AR-PAM, and the axial resolution of OR-PAM. In addition, the pulse width is related to the generated PA signal amplitude at the target. As shown in Fig. 1.4a, when the stress confinement is not satisfied, i.e., the excitation pulse is long compared with the stress confinement, the resultant PA pressure at the target is roughly inversely proportional to the square of the pulse width [85, 101]. In this sense, a shorter pulse is more efficient in generating PA signals than a longer pulse. However, the increased PA signal mostly falls into the high-frequency region. As we know, after the low-pass filtering by tissue, high-frequency acoustic components will not be captured by the ultrasonic transducer. As can be seen from Fig. 1.4a, once the stress confinement is satisfied, the excitation pulse can be approximated

as a delta function, and the resultant PA pressure at the transducer surface relies only on the excitation pulse energy and is not sensitive to the pulse width anymore. Therefore, it is not necessary to further reduce the pulse width once the targeted signal bandwidth is matched. The pulse width needs to be optimized according to the desired spatial resolution or imaging depth. Furthermore, because excitation intensity is pulse width related, pulse width also affects PA signal generation through the absorption saturation effect [101].

Moreover, the biological systems were usually studied on both macroscopic and microscopic scales. By adjusting the excitation and detection configurations, all of the key imaging parameters of PAM, including spatial resolution, imaging depth, and detection sensitivity, can be scaled over a wide range with the same optical absorption contrast. Such high scalability is critical for comprehensive study of biological phenomena over different length scales and for the translation of laboratory discovery to clinical practice. Comprehensive details about PAM characterizations and biomedical applications can be found in previous review articles [40, 62, 85], and a summary of the scalable imaging performance of representative PAM systems is shown in Fig. 1.4b. To achieve the ultimate detection sensitivity, PAM needs to optimize its optical illumination and acoustic detection, based on the desired imaging specifications.

1.3 PAM Implementations

As discussed in the introduction, PAM systems are usually divided into two categories: AR-PAM and OR-PAM, as shown in Fig. 1.5. Both systems present different lateral resolutions and penetration depths. In this section, we describe several representative system configurations and discuss their characteristics, which may help to understand the two available PAM systems in more detail. While we present acoustic-resolution and optic-resolution systems as distinct PAM systems here, it should be noted that in some cases, OR- and AR-PAM are interchangeable, and merging the two systems together is possible to achieve a dual-illumination system [108, 109]. In PAM, the PA signals are formed at the co-focal point of light and acoustic wave. Aligning two beams coaxially is important to maximize the sensitivity of PAM, which has been realized through the design of many technologies. Various types of PAM systems are summarized in Fig. 1.6.

Off-axis alignment is an easy way to implement an acoustic-optic combiner. However, this method system has limited detection sensitivity and FOV, so it is difficult to implement in AR-PAM systems. Additionally, the misalignment of light and acoustic waves further limits the axial resolution of imaging. Due to these features, the off-axial PAM system is mainly used for the imaging of flat plane samples or very small FOV [110, 111]. Dark-field confocal PAM is another popular system in which a conical lens is used to form an annular-shaped light beam that can bypass the acoustic detector [112, 113]. The light illuminates the sample at a tilted angle, and the transducer collects the generated acoustic wave above the sample.

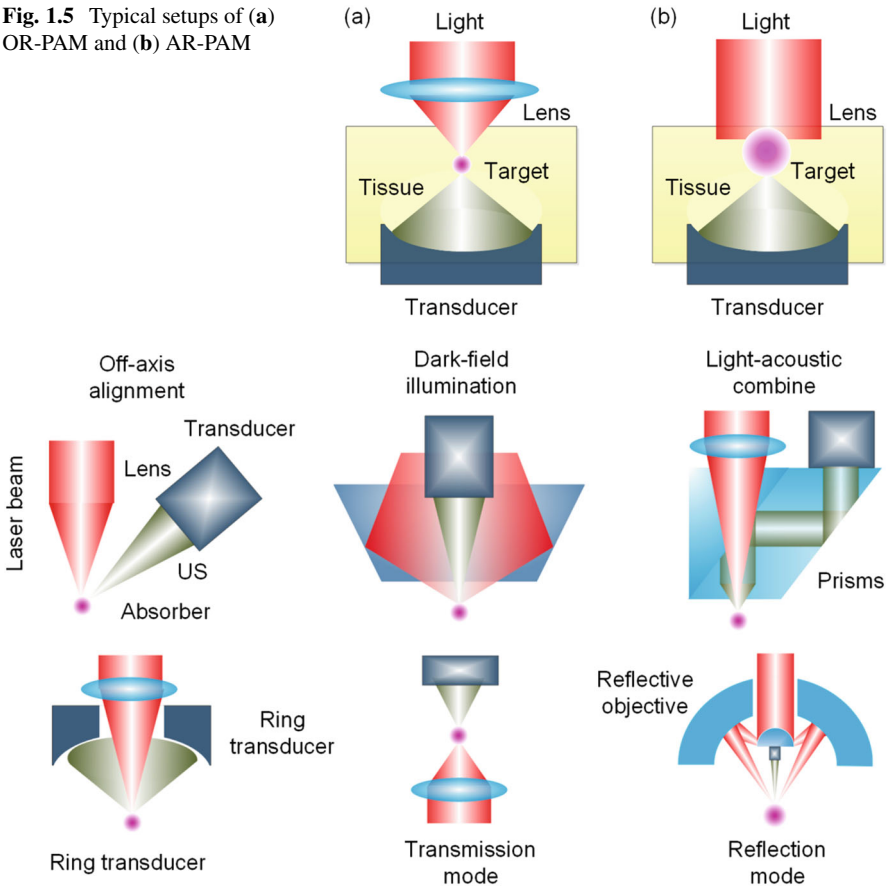

Fig. 1.5 Typical setups of (**a**) OR-PAM and (**b**) AR-PAM

Fig. 1.6 Features of various PAM implementation types. NA numerical aperture, AR acoustic resolution, and OR optical resolution [109]

This coaxial configuration can result in a high SNR. However, because the light cannot be focused tightly, it is only appropriate for use in AR-mode imaging. Like AR-PAM, AR-mode imaging is usually used to visualize larger and deeper targets. The second-generation combiner typically utilizes a glass plane (transparent to light and reflective of acoustic waves) to combine light and acoustic waves together, making them coaxial [114, 115]. This method can focus tightly to get a high lateral resolution less than 5 μm, and presents a considerable imaging depth of 1.2 mm. One of the primary drawbacks of this method is that some acoustic energy will likely be lost thanks to the acoustic impedance mismatch of the combiner. In spite of its drawbacks, this method has been a popular technology used in OR-PAM, AR-PAM, and even a switchable system in in vivo microscopy. In the fourth method, a ring transducer is used, which has a hole for light to pass through [116]. The PA signal is then detected on the other side of light source. This method aligns light and acoustic